

PERFORMANCE IMPROVEMENT OF A COMPOUND HELICOPTER ROTOR HEAD BY AERODYNAMIC SHAPE OPTIMIZATION

P. Pözlbauer* , D. Desvigne** , C. Breitsamter*
*Technical University of Munich , **Airbus Helicopters

Keywords: *Design Optimization, CFD, Helicopter Aerodynamics, Blade-Sleeve Fairing, RACER*

Abstract

Within the present publication, the rotor head of a compound helicopter known as Rapid And Cost-Effective Rotorcraft (RACER) is investigated. In particular, the aerodynamic design optimization of the RACER blade-sleeve fairings is conducted. For this purpose, an isolated rotor head is generated featuring a full-fairing beanie, the blade-sleeve fairing and a truncated rotor blade. Moreover, a steady rotor is investigated and averaged flow conditions according to the RACER cruise flight are applied. The automated aerodynamic design optimization is performed by means of a previously developed optimization tool chain. A global multi-objective genetic optimization algorithm is applied for the given problem. During preliminary work, a two-dimensional aerodynamic design optimization of selected blade-sleeve sections was conducted. These optimized airfoils represent the design variables for the current optimization problem. The shape modification of the three-dimensional fairing is realized by exchanging specific airfoils at certain spanwise sections.

1 Introduction

Europe and its aviation industry have defined very ambitious goals regarding the development of future air transportation concepts. The reduction of the environmental impact as well as the performance improvement of future vehicles are the key challenges to be tackled. Especially, the

reduction in CO₂ and NO_x emissions as well as the decrease of the noise footprint are in focus. At the same time, a seamless door-to-door mobility is required by the growing population. However, conventional aircraft require a large ground infrastructure and rotorcraft do not achieve the cruising speed, payload and range of such an aircraft. Therefore, the gap between those two configurations can only be closed by the development of a novel aircraft concept. One of these concepts is represented by the new compound helicopter configuration known as Rapid And Cost-Effective Rotorcraft (RACER), which is developed within the European Clean Sky 2 Joint Technology Initiative (CS2-JTI). The RACER combines the beneficial characteristics of a fixed-wing aircraft with the ability of a helicopter for vertical take-off and landing (VTOL). Furthermore, the predicted cruising speed is around 220 knots, which is approximately 50 percent higher than for a conventional helicopter. Due to the high cruising speed, aerodynamic efficiency becomes an important topic during the RACER development. Regarding a conventional helicopter, the rotor head represents a major drag source, which offers potential in terms of drag reduction. Hence, one possibility is to design fairings for certain rotor head components, which was comprehensively investigated within the Clean Sky Green RotorCraft Research Program [1, 2].

Moreover, the importance of hub drag minimization is reflected by a large number of experimental [3, 4, 5] and numerical investigations [6, 7] that have been conducted over the last decades. The present work is related to the Clean Sky 2 project FURADO (Full Fairing Rotor Head Aerodynamic Design Optimization), which deals with the aerodynamic design optimization of a semi-watertight full-fairing rotor head by means of CFD simulations. For this purpose, the rotor-head fairings are divided into three main components, the blade-sleeve fairing, the full-fairing beanie and the pylon fairing. The present publication deals with the aerodynamic design optimization of the RACER blade-sleeve fairing. During preliminary work, two-dimensional airfoils were aerodynamically optimized for selected sections of the blade-sleeve fairing. These airfoils yield a database of supporting geometries, which are used for the modification of the three-dimensional fairing shape. Furthermore, a global multi-objective genetic optimization algorithm is applied and selected supporting airfoils represent the design variables for the given optimization problem.

2 RACER Compound Helicopter

The innovative demonstrator RACER provides a concept allowing to expand the flight envelope of helicopters towards higher cruising speeds. The development of this new configuration is based on the experience gained through the X³ demonstrator program of Airbus Helicopters [8]. It offers a common demonstrator platform for new technologies and it is developed within a European framework of industrial and academic partners. Figure 1 gives an overview on the RACER compound helicopter configuration. The main differences, compared to a conventional helicopter, are given by the innovative box-wing design holding two lateral rotors as well as the horizontal and vertical stabilizers in H-type architecture. Moreover, a classical five-bladed main rotor is used enabling vertical take-off and landing. Concerning cruise flight, a significant part of the lift is generated by the wings. Hence, the main

rotor can be unloaded and its rotational speed is decreased, which keeps the tip Mach-number of the advancing rotor blade low enough to avoid transonic effects. Furthermore, the stabilizers are equipped with rudders and provide pitch and yaw stability during cruise flight. The propellers deliver additional thrust, generate anti-torque and enable yaw control in hover.



Fig. 1 : Clean Sky 2 demonstrator RACER [9].

The expected RACER performance is defined by a 50% higher cruising speed and a cost reduction of 25% per nautical mile compared to conventional helicopters from the same class. Considering the high cruising speed, aerodynamic efficiency becomes an important topic during the RACER development. Especially drag reduction is one of the major challenges to be tackled in order to achieve the predicted goals. Therefore, highly efficient wings, a low-drag fuselage and a fully faired main rotor are employed.

3 Geometry

Within the present publication, the aerodynamic design optimization of the RACER blade-sleeve fairing is at focus. Figure 2 shows a simplified CAD model of the rotor head, which consists of three components. These include the full-fairing beanie (FFB) in green, the blade-sleeve fairing (BSF) in orange and a truncated rotor blade (RB) in blue. Hence, an isolated rotor head is taken into account and its interference effects with the fuselage as well as the pylon fairing are neglected.

Additionally, the dampers between the rotor blades are omitted, which reduces the complexity in terms of mesh generation. The junction between the blade-sleeve fairing and the full-fairing beanie as well as the transition to the rotor blade are geometrically fixed. Hence, these sections keep their shape throughout the optimization process. Furthermore, the cross-sections of the supporting airfoils, which represent the basis for the three-dimensional blade-sleeve fairing, are depicted in Fig. 2. The shape variation of the blade-sleeve fairing is achieved by replacing the supporting airfoils. For this purpose, a database of selected two-dimensional geometries is employed, which was generated during previous work within the FURADO project [10]. The four supporting airfoils (S1-S4) are located in a region of $0.078 \leq r/R \leq 0.149$, where R corresponds to the rotor radius.

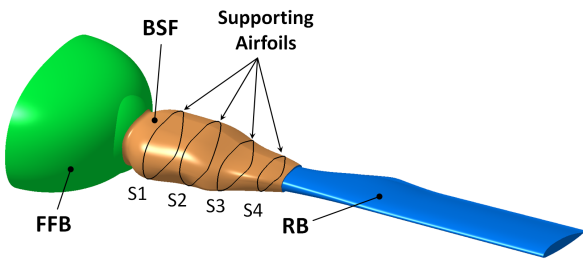


Fig. 2 : CAD model applied for the design optimization of the RACER blade-sleeve fairing.

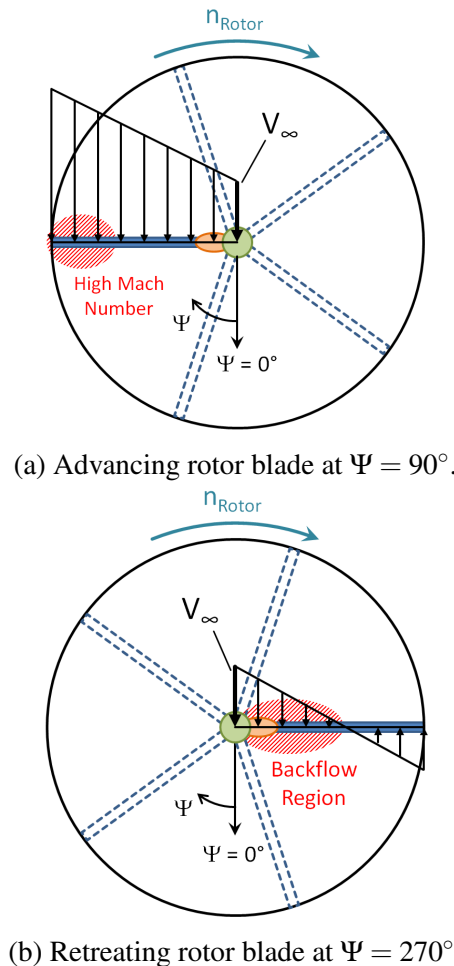
4 Optimization Approach

Within this section, the aerodynamic design optimization process for the RACER blade-sleeve fairing is described. This includes an introduction to the applied optimization tool chain, a description of the optimization problem and a brief overview on the selected optimization algorithm. A general introduction to optimization formulation and different optimization techniques is given in [11]. During the first phase of the FURADO project, the optimization tool chain allowing for fully automated aerodynamic shape optimization was developed. It consists of five main modules, which can be divided into optimization,

shape generation, mesh generation, flow simulation and design evaluation. A detailed description of the applied tool chain is provided in [10].

4.1 Optimization Problem

During preliminary work, the two-dimensional blade-sleeve sections were aerodynamically optimized for cruise flight, which is the most relevant flight condition in terms of drag reduction. For this purpose, the local flow conditions for each section were taken into account, which vary due to the circumferential velocity and the flow deflection caused by the fuselage. Two different azimuthal positions of the rotor were investigated, which are shown in Fig. 3 and correspond to the advancing and retreating rotor blade.



(a) Advancing rotor blade at $\Psi = 90^\circ$.

(b) Retreating rotor blade at $\Psi = 270^\circ$.

Fig. 3 : Comparison of the flow conditions for the investigated azimuthal rotor positions.

Previous investigations at TUM-AER revealed that the highest drag values are obtained at these azimuthal rotor positions [12]. Typical flow-velocity profiles for cruise flight are given in Fig. 3a and Fig. 3b. The flow conditions are characterized by high Mach numbers in the tip region of the advancing rotor blade and a back-flow region in the vicinity of the rotor axis for the retreating rotor blade. Regarding the RACER demonstrator, the rotational speed of the main rotor is adapted for each flight condition to keep the tip Mach number within a permissible range during cruise flight and to provide sufficient lift during hover. The design optimization of the two-dimensional blade-sleeve sections represents the basis for the current optimization problem. Therefore, similar objective functions are applied and their mathematical description is given by Eq. 1 and Eq. 2. The main objective is to reduce the drag caused by the blade-sleeve fairings during cruise flight. However, lift is taken into account as well in the objective function for the advancing rotor blade. In terms of overall drag, any additional lift generated by the blade-sleeve fairings would have a beneficial effect on the entire configuration. Moreover, the minimization of drag is considered as the objective function for the retreating rotor blade, which is located within a back-flow region.

$$\text{maximize } f_1(\mathbf{x}) = C_L/C_D \quad (\text{Adv. Blade}) \quad (1)$$

$$\text{minimize } f_2(\mathbf{x}) = C_D \cdot S \quad (\text{Ret. Blade}) \quad (2)$$

Four discrete design variables representing specific geometries of the supporting airfoils are applied:

$$\mathbf{x} = \{S_1, S_2, S_3, S_4\} \quad (3)$$

For each section (S_1 - S_4), twelve airfoils originating from the two-dimensional design optimization are selected. Figure 4 exemplarily shows the objective space for the final population of one blade-sleeve section. Both objective functions are normalized by a symmetric reference geometry. The designs close to the Pareto

front can be divided into three main regions. Designs with low drag values regarding the retreating blade case are located in the blue colored region and geometries offering a compromise between both objective functions can be found in the orange colored region. Moreover, the green colored region contains designs with high lift-to-drag ratios concerning the advancing blade case. From each of the three regions, four airfoils are selected for each of the blade-sleeve sections. Hence, a database containing 48 optimized airfoils is created, which corresponds to 20736 possible shape combinations. Evaluating all possible shapes of the blade-sleeve fairing is not possible within a reasonable time-frame. Hence, a multi-objective design optimization is employed to find a feasible geometry. During the preliminary optimization of the blade-sleeve sections, design constraints regarding the available design space were applied. Therefore, these constraints are automatically met by the three-dimensional blade-sleeve fairing and an unconstrained optimization can be performed.

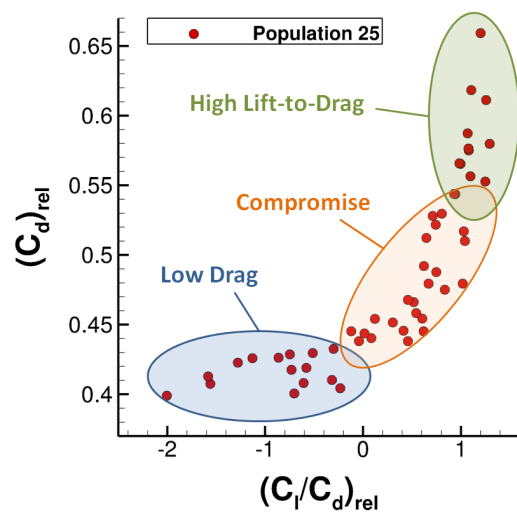


Fig. 4 : Exemplary objective space for the final population of the two-dimensional design optimization showing the three main regions of the Pareto front.

4.2 Optimization Algorithm

The selection of the optimization algorithm for a given optimization problem is based on the characteristics of the design space and the applied constraints. In convex search spaces, gradient-based optimization algorithms efficiently navigate into a local optimum close to the starting point. However, these algorithms are not suited for multi-modal problems, because they could get caught in such a local optimum. Therefore, derivative-free global evolutionary algorithms offer a robust alternative in non-convex search spaces or whenever the characteristics of the search space are unknown. However, global optimization algorithms require a large number of function evaluations compared to gradient-based algorithms. Concerning the present optimization problem, similar concurring objective functions as for the two-dimensional design optimization are employed. However, they slightly differ, because the force-coefficients are multiplied by the reference surface S for the three-dimensional investigations. Moreover, the flow around the rotor head fairing represents a complex flow problem and the properties of the search space are unknown. Therefore, a robust multi-objective genetic algorithm (MOGA) is used for the aerodynamic design optimization of the RACER blade-sleeve fairing. Genetic algorithms (GAs) use the principles of natural selection, which means that they are based on Darwin's theory of survival of the fittest. These algorithms start their search for the optimal solution from a population of designs and not from a single one. In combination with a parameter sampling method, which is applied for the initialization of the first population, a wide range of the design space can already be covered at the beginning of the optimization process. Moreover, GAs only use objective functions to determine the fitness of a design. Hence, they do not require any auxiliary information, like gradients or Hessians. The transition from one population to a subsequent one depends on probabilistic rules.

The main operations used within a GA are reproduction, crossover and mutation. Depending on the objective function of a candidate, it has a certain probability of being selected for contributing offspring in the next generation. Within the next step, a mating pool of candidates is generated and they are combined in pairs crossing over genetic information. Additionally, a mutation operator is employed to randomly change the values of coded design variable strings in order to prevent the optimization algorithm from losing important genetic information [13, 14].

5 Numerical Setup

Within this section an overview on the investigated flow conditions, the computational mesh and the applied flow solvers is given. As mentioned in Sec. 4.1, two different flow conditions are examined yielding the advancing and retreating rotor blade case. In order to simplify the optimization process, a stationary rotor is investigated. Therefore, an averaged circumferential velocity is superposed with the cruise speed of the helicopter, which corresponds to $V_{Cruise} = 220$ kts. Furthermore, an averaged angle of attack is applied for all sections, which is defined by the collective pitch, the longitudinal cyclic-pitch and an averaged local angle of attack due to the flow deflection of the fuselage. Additionally, the employed ambient conditions are representative for a sea-level cruise flight in ICAO standard atmosphere [15].

5.1 Computational mesh

The applied computational mesh is generated with Ansys ICEM. A block-structured hexahedral mesh consisting out of 182 blocks is created. The dimensions of the computational domain are illustrated in Fig. 5. The quantity d_{FFB} represents the diameter of the full-fairing beanie, which is shown in green. The size of the domain is big enough to ensure that no influence from the imposed boundary conditions can be observed in the flow field near the geometry.

In order to minimize the computational time on the one hand and to ensure low numerical dissipation due to the spatial discretization on the other hand, mesh independence studies were conducted to find the required mesh size. As a result, a computational mesh featuring 7.2 million elements was selected for the numerical investigations. Furthermore, the boundary layer is fully resolved by selecting a dimensionless wall distance of $y^+ \approx 1$ for the initial cell height and a mesh expansion ratio of 1.2. On the front, top, back and bottom of the computational domain, farfield boundary conditions are applied. A symmetry boundary condition is used on the surface connected to the investigated geometry. For the remaining side of the domain, a free-slip wall is chosen. The initial mesh is generated for a baseline geometry of the blade-sleeve fairing, which uses airfoils yielding the best compromise of both objective functions. Subsequent meshes are automatically generated by updating the geometries and reassociation.

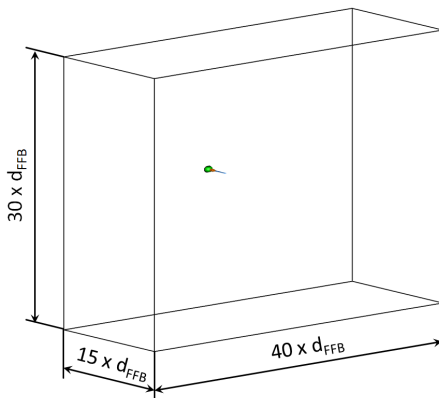


Fig. 5 : Computational domain used for the CFD simulations.

5.2 Flow solvers

This section summarizes the numerical setup of the applied flow solvers. Ansys FLUENT as well as the DLR TAU-Code were used for the numerical investigations within the present publication. The preliminary aerodynamic design optimization of the blade-sleeve fairing sections was conducted using Ansys FLUENT. Further-

more, all time-accurate results for detailed analysis were produced with this flow solver, because faster convergence was observed in terms of unsteady flow simulations. The DLR TAU-Code was employed for the three-dimensional design optimization of the blade-sleeve fairing.

5.2.1 ANSYS Fluent

The numerical flow simulations dealing with the two-dimensional design optimization of the blade-sleeve fairing sections were conducted with Ansys FLUENT. Furthermore, selected three-dimensional blade-sleeve fairing designs were investigated with this flow solver. Due to Mach numbers within a range of 0.3-0.4, compressibility effects are taken into account. Therefore, the compressible, unsteady Reynolds-Averaged Navier-Stokes equations (URANS) are considered. The initialization of the transient flow simulation is performed by the application of a steady state solution. Furthermore, the $k-\omega$ SST model [16] is employed for turbulence modeling. Moreover, the SIMPLEC algorithm is applied for the treatment of pressure-velocity coupling, which allows for increased under-relaxation. The pressure interpolation is achieved by the standard pressure scheme of FLUENT. Regarding the spatial discretization, second-order upwind schemes are chosen for density, momentum, turbulent kinetic energy, specific dissipation rate and energy. Further, a least-squares cell-based formulation is applied for the gradient calculation and a bounded second-order implicit scheme is used for the temporal discretization [17]. The time-step size for the time-accurate simulations was set to $\Delta t = 10^{-4}$ s, which corresponds to a resolution of 130 points per period regarding the observed oscillation of forces. Furthermore, all normalized residuals were reduced by at least four orders of magnitude. Depending on the investigated geometry, this was achieved within approximately ten inner iterations per time step. During preliminary tests regarding the simulation setup, it was observed that doubling the time-step size leads to approximately 60 percent more inner iterations.

Further, a more stable setup could be obtained with the smaller time-step. The applied fluid is air ideal gas and its properties are set according to a sea-level cruise flight.

5.2.2 DLR TAU-Code

The numerical investigations for the evaluation of the objective functions concerning the three-dimensional design optimization are conducted with the DLR-TAU Code. This CFD solver was developed at the DLR (German Aerospace Center) and solves the compressible steady or unsteady Reynolds-Averaged Navier-Stokes (RANS) equations. The flow calculation is based on a dual grid approach and a cell vertex grid metric is employed. Turbulence modeling is achieved by the SST k-g model, which represents a re-implemented version of the Menter SST model [16, 18]. The standard TAU average of flux central scheme is selected for the discretization of the meanflow equations. Furthermore, a Roe second-order scheme is applied for the convective fluxes of the turbulence equations and a Green-Gauss algorithm is chosen for the gradient reconstruction. The system of equations is solved by a Lower-Upper Symmetric-Gauss-Seidel (LU-SGS) method and scalar dissipation is used for the numerical dissipation scheme. An overview of the hybrid RANS solver TAU is given in [19]. Regarding the convergence of the flow simulations, the normalized density residual was reduced by three orders of magnitude.

6 Results

The present section introduces the applied optimization setup and shows the intermediate results of the currently ongoing blade-sleeve fairing optimization. The Automated Aerodynamic Shape Development (AASD) tool chain, which was developed at TUM-AER, was used in combination with a multi-objective genetic algorithm to generate the data.

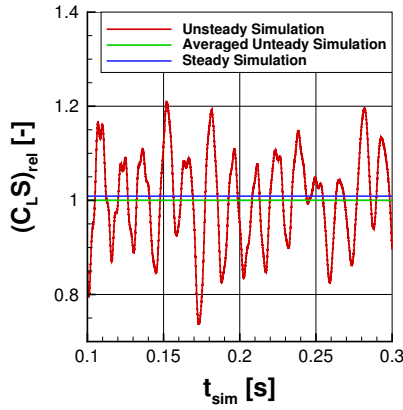
The investigated objective functions are given by the maximization of the lift-to-drag ratio (C_L/C_D) for the advancing rotor blade ($\Psi = 90^\circ$) and the minimization of drag $C_D S$ for the retreat-

ing rotor blade ($\Psi = 270^\circ$). Four discrete design variables, which correspond to specific designs from an airfoil database, span the available design space. Twelve airfoils were selected for each section, which yields a design variable range of $1 \leq S_1, S_2, S_3, S_4 \leq 12$. Regarding the ranking of the designs, a domination count is used to order the population members and to determine their fitness. One design is dominating another one, if it is better in both objective functions. The designs that are kept for the subsequent generation are selected by a below limit replacement value of six. This means that the number of candidates dominating a specific design has to be lower than the replacement value, otherwise this design is rejected. Furthermore, the reduction of the population size is controlled by a shrinkage percentage of 95%. This value specifies the number of candidates, which have to continue to the next generation. Hence, it prevents an excessive decrease in the population size. Furthermore, the below-limit selector is adapted, if the algorithm does not find sufficient designs to fulfill the shrinkage percentage requirement. Additionally, a differentiation along the Pareto-frontier is achieved by employing niching during the optimization. The initial population contains 150 designs, which were randomly generated by the applied optimization tool-box DAKOTA [20]. Regarding the optimization results, an evaluation of the objective space is conducted and one design is selected to be investigated in more detail. Moreover, an overview on the prevailing flow field is given and the occurring flow phenomena are described. For this purpose, a baseline design is introduced, which features airfoils offering the best compromise between the objective functions from the two-dimensional design optimization.

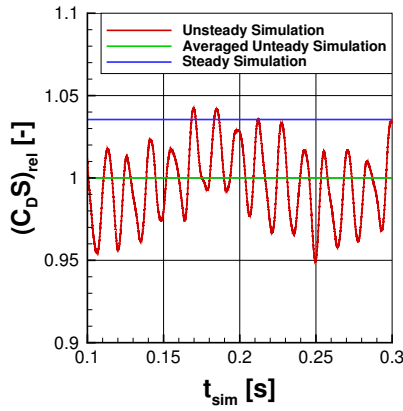
6.1 Evaluation of the objective space

Within this section, the evaluation of the blade-sleeve fairing designs is presented. The investigated geometry yields a bluff body and an unsteady flow field can be observed in its wake region.

However, time-accurate flow simulations require a significant amount of time, which is undesired in terms of the automated design optimization. Therefore, a comparison between a time-accurate and a steady-state flow simulation was conducted for a representative test-case using the DLR-TAU Code. Figure 6 shows the results for the time-accurate simulation (red), the averaged time-accurate simulation (green) and the steady-state simulation (blue). All results are normalized with the final value of the averaged time-accurate simulation.



(a) Normalized lift coefficient $(C_L S)_{rel}$.



(b) Normalized drag coefficient $(C_D S)_{rel}$.

Fig. 6 : Comparison of an averaged time-accurate flow simulation with the results from a quasi steady-state flow simulation.

The total simulation time was $T_{sim} = 0.3$ s and the applied time-step was $\Delta t = 2 \cdot 10^{-4}$ s. Regarding the normalized lift-coefficient $(C_L S)_{rel}$, which is illustrated in Fig. 6a, a deviation of 0.9 percent can be observed between the steady-

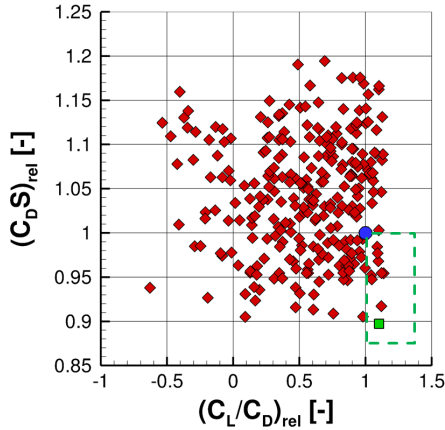
state and the averaged time-accurate simulation. Furthermore, a difference of 3.5 percent was obtained for the normalized drag-coefficient $(C_D S)_{rel}$, which is shown in Fig. 6b. The deviation from the time-accurate simulation is considered to be within a reasonable range and therefore, a steady-state simulation setup is used for the current optimization task. A steady-state flow simulation with 22000 iterations is performed to calculate the objective functions for the design evaluation. During the first phase of the design optimization, 334 designs have been evaluated. An overview on the objective space is given in Fig. 7. Both objective functions are normalized with reference values from the baseline design of the blade-sleeve fairing. Hence, the performance of a candidate is evaluated relative to this reference geometry. The feasible objective space is defined in a region of $-0.63 \leq (C_L/C_D)_{rel} \leq 1.14$ and $0.89 \leq (C_D S)_{rel} \leq 1.2$. Furthermore, the baseline design, which is located at $(C_L/C_D)_{rel} = 1$ and $(C_D S)_{rel} = 1$, is marked with a blue symbol. Any design that is better than the reference, is located within the highlighted region, in the bottom-right corner of Fig. 7a. A detailed view on the currently best performing designs is given in Fig. 7b. Candidate C1 achieves the highest lift-to-drag ratio $(C_L/C_D)_{rel}$ and candidate C2 provides the lowest drag $(C_D S)_{rel}$. The relative performance improvement of C1 and C2 is summarized in Table 1.

Design	f_1	f_2	Δf_1 [%]	Δf_2 [%]
C1	1.136	0.954	+13.6	-4.6
C2	1.101	0.897	+10.1	-10.3

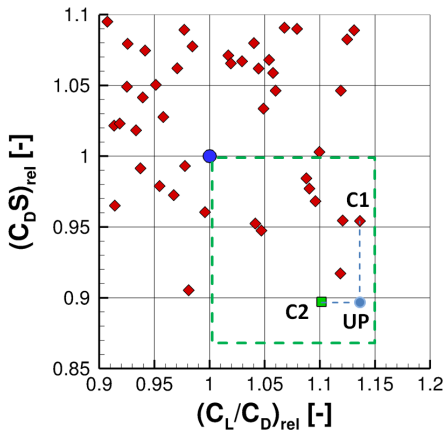
Table 1: Comparison of the objective functions for the designs C1 and C2.

Connecting the designs C1 and C2 leads to the utopia point UP for the current set of results. This point represents a theoretical design that combines the best of both objective functions. However, this point cannot be reached, because there is always a trade-off between the concurring objective functions.

The distance between UP and any other design is taken into account to find a geometry, which offers a good compromise between both objective functions. The geometry with the smallest distance to UP is given by candidate C2, which is marked by a green symbol in Fig. 7. Moreover, this design is investigated in more detail and compared to the baseline geometry.



(a) Overview on the entire objective space.



(b) Detailed view on the designs featuring the best objective functions.

Fig. 7 : Objective space showing the evaluated designs from the multi-objective design optimization.

In order to exemplarily show the difference between the baseline geometry and the selected design C2, the chordwise pressure distribution is determined at the second radial blade-sleeve section S2. This section was chosen, because only

minor interference effects with a large flow separation originating from the transition region between the full-fairing beanie and the blade-sleeve fairing are present. The sectional shapes of the baseline design and candidate C2 are depicted in Fig. 8. Additionally, the design constraints, which were applied during the two-dimensional design optimization, are shown by red and blue lines. It can be observed that both designs are close to the minimum permissible design space.

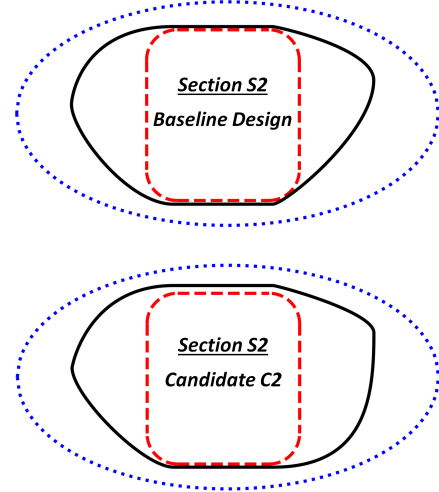
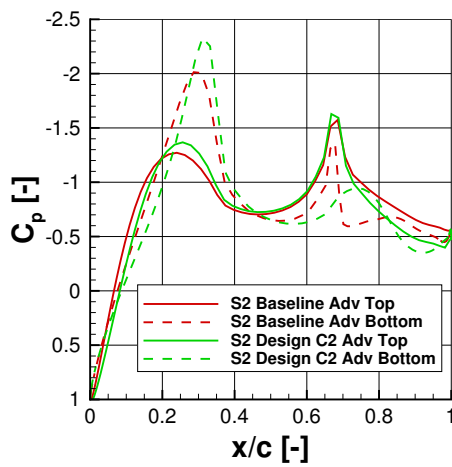


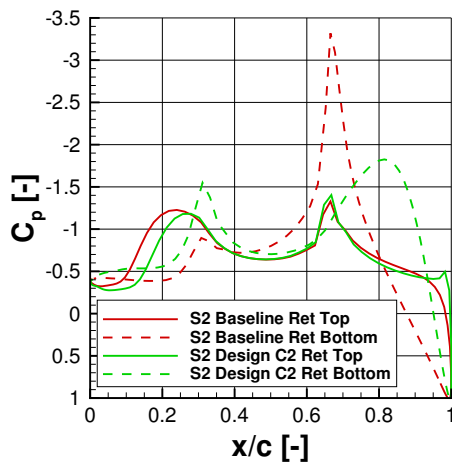
Fig. 8 : Comparison between the sectional shapes of the baseline design and candidate C2 at the radial position S2.

Figure 9 shows the chordwise pressure distribution $C_p(x/c)$ for the selected candidate C2 in comparison to the baseline design. The data was extracted from the second radial section S2. The results for the advancing rotor blade are shown in Fig. 9a and for the retreating rotor blade they are given in Fig. 9b. The pressure distribution in Fig. 9b is mirrored, because reversed flow is present for the retreating blade. Regarding the pressure distribution on the upper surface of the blade-sleeve fairing, which is represented by solid lines in both figures, no big differences can be observed. This is caused by the fact that the contour on the upper surface is quite similar for both designs. Hence, the same suction peak can be observed at $x/c = 0.65$ for the advancing and the retreating rotor blade, which is related to a strong curvature in the geometry.

Concerning the bottom surface of the baseline design in Fig. 9a, a pressure drop can be identified at 70 percent of the chord-length, which is related to a region of separated flow. The onset of flow separation is triggered by a strong curvature at $x/c = 0.7$. Furthermore, the smoothed contour of the optimized design C2 leads to a delayed flow separation within this region. Considering the retreating blade case in Fig. 9b, a significant suction peak can be seen on the lower surface of the baseline design. In comparison to this, moderate pressure levels are obtained for candidate C2.



(a) Advancing rotor blade.



(b) Retreating rotor blade.

Fig. 9 : Comparison of the chordwise pressure distribution between the baseline design and the selected candidate C2 at section S2.

6.2 Flow field visualization and 3D effects

At first, a general view on the prevailing flow field and the occurring flow phenomena is given. For this purpose, the simulation results of the baseline design are shown, which are representative for candidate C2 as well. The flow field is visualized by means of the averaged, axial flow velocity $V_{X,mean}$, which is normalized by the free-stream velocity V_∞ . Figure 10 shows four slices in chordwise direction, which are located within a range of $0.5 \leq x/c \leq 1.5$. Moreover, the results for the advancing and the retreating rotor blade are illustrated in Fig. 10a and Fig. 10b. The cutoff values for the contour plots are set according to $(V_{X,mean}/V_\infty)_{min} = 0$ and $(V_{X,mean}/V_\infty)_{max} = 1$. Additionally, an iso-surface is drawn at $V_{X,mean}/V_\infty = 0$ for both cases. By means of this iso-surface, a large region of separated flow can be identified, which features reversed flow inside. The onset of flow separation is located in the transition region between the blade-sleeve fairing and the full-fairing beanie, at approximately half of the chord length. Furthermore, the first blade-sleeve section S1 is influenced by this flow separation and reduced pressure levels are obtained compared to the two-dimensional simulation results. Moreover, the flow separation is larger for the retreating blade case, which can be seen in Fig. 10b. Starting from a spanwise position of $y/l_y = 0.5$, almost undisturbed wake flow fields can be observed. Furthermore, y-slices showing the averaged and normalized axial flow velocity are depicted in Fig. 11. These slices are located at the radial positions of the four supporting airfoils (S1-S4). In comparison to the wake flow field of section S1, the region of reduced axial flow velocity is much smaller for the remaining sections S2-S4. In Fig. 11b, the results for the retreating rotor blade are shown. Concerning section S3, it can be observed that the flow separates earlier on the bottom surface, which leads to a flow deflection in downward direction. Additionally, the velocity deficit is more pronounced for the sections S1 and S2 compared to the advancing blade case in Fig. 11a.

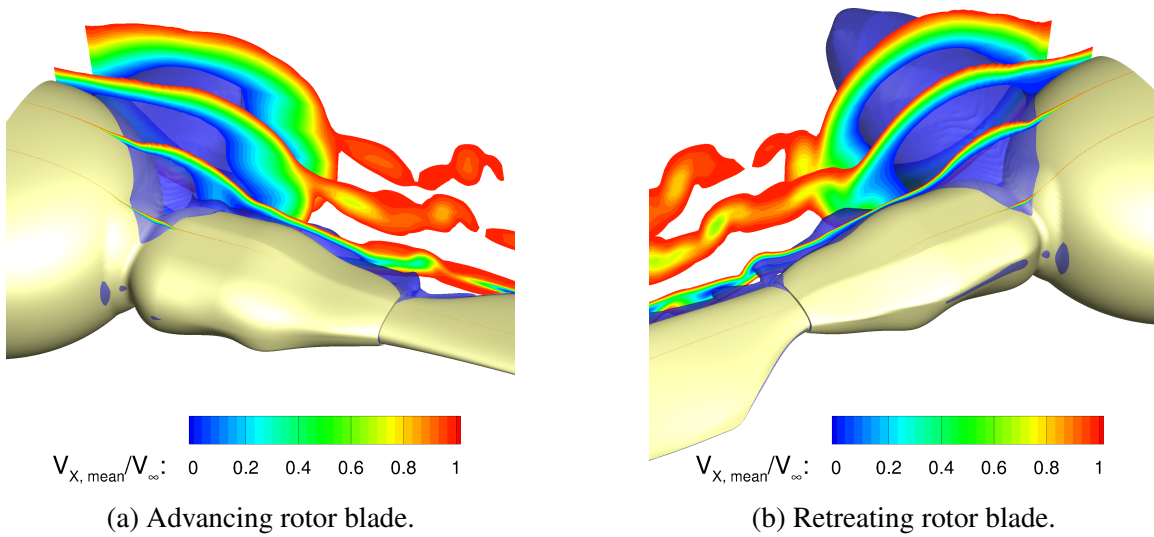


Fig. 10 : Baseline Fairing: Normalized axial flow velocity $V_{X, \text{mean}}/V_{\infty}$ shown at four evenly distributed x-slices within the region $0.5 \leq x/c \leq 1.5$.

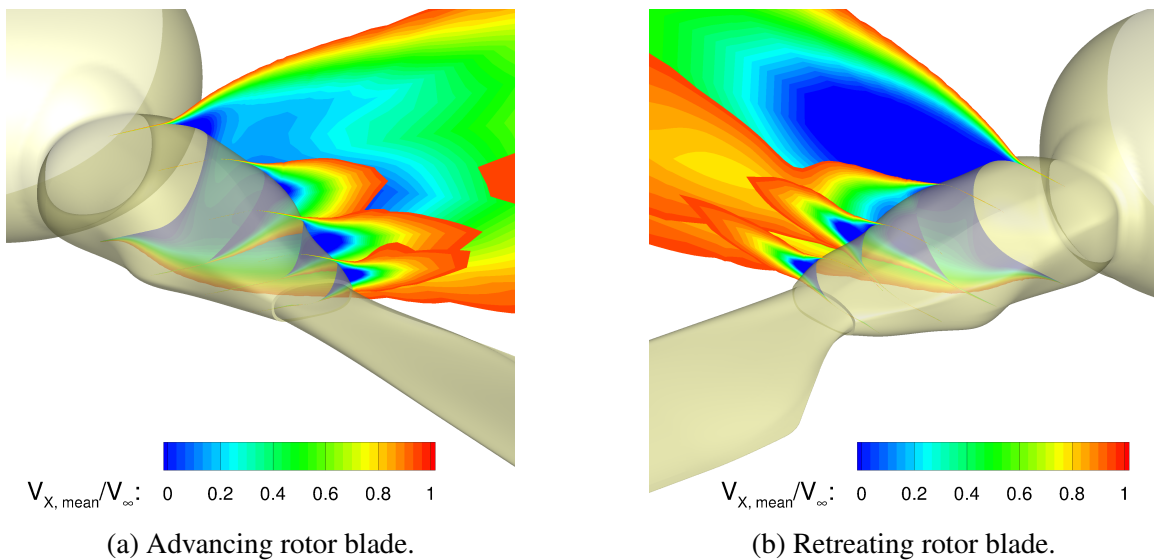
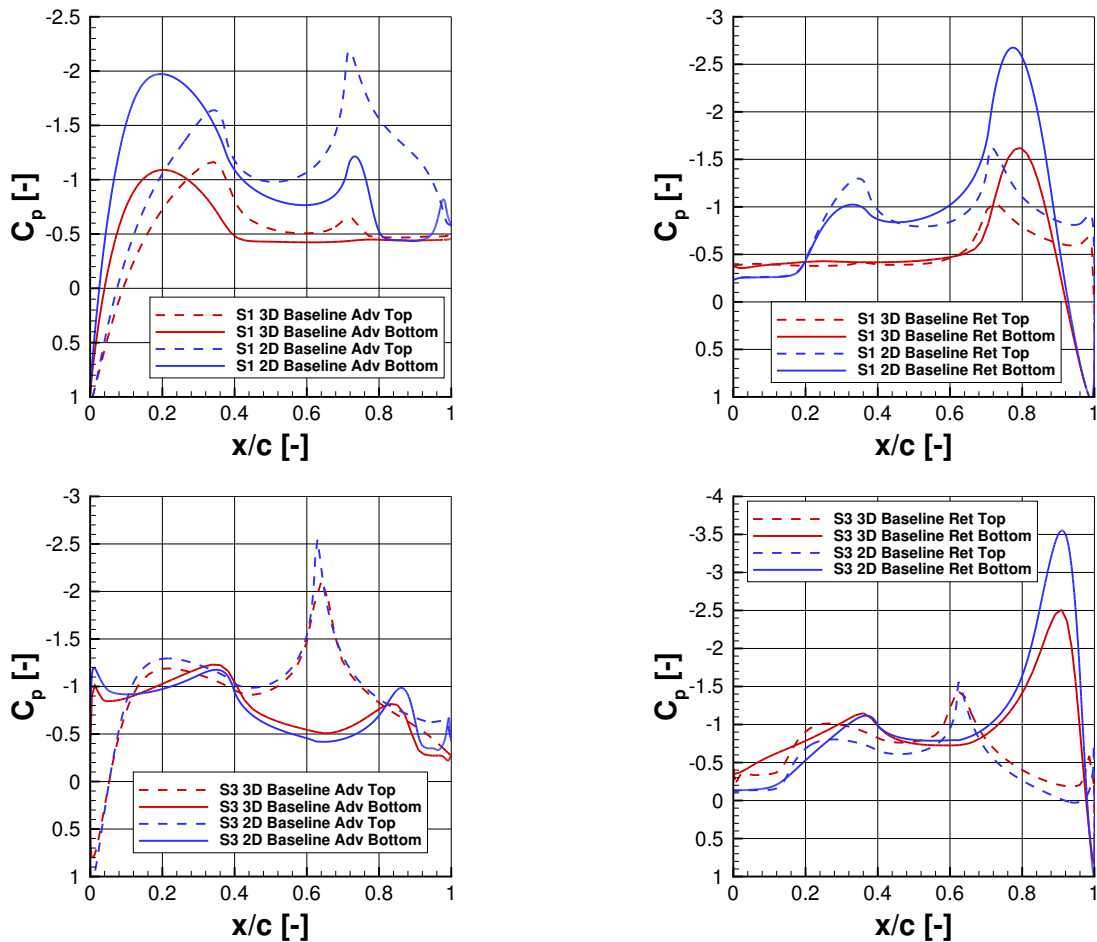


Fig. 11 : Baseline Fairing: Normalized axial flow velocity $V_{X, \text{mean}}/V_{\infty}$ shown at the four blade-sleeve sections S1-S4.

In order to determine the influence of the three-dimensional effects, the results from the preliminary airfoil optimization are compared to the results from the three-dimensional flow simulations. For this purpose, the chordwise pressure distributions are considered for the sections S1 and S3, which can be seen in Fig. 12. Regarding section S1, a large discrepancy between the airfoil pressure distribution and the three-dimensional result is present. The flow field

in this region is dominated by the flow separation between the blade-sleeve fairing and the full-fairing beanie, which strongly influences the pressure distribution at this spanwise location. Hence, almost constant pressure is obtained over 60 percent of the chord length for the advancing as well as the retreating blade case.



(a) Advancing rotor blade.

(b) Retreating rotor blade.

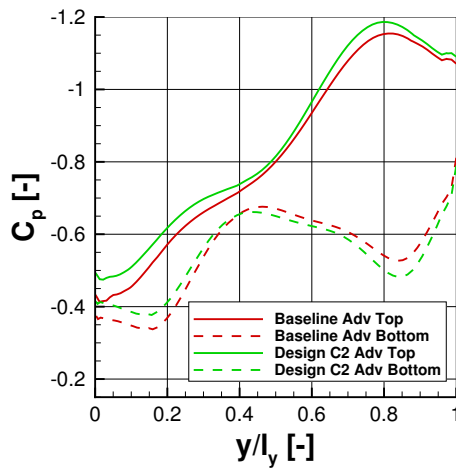
Fig. 12 : Comparison of the two-dimensional (2D) and the three-dimensional (3D) simulation results considering the pressure distribution $C_p(x/c)$ at the sections S1 and S3.

Regarding the pressure distributions of section S3, good agreement between the two-dimensional (2D) and three-dimensional (3D) results can be observed for both cases. However, a significant difference can be identified in the front region of the bottom surface for the retreating blade case, which is depicted in Fig. 12b. Nevertheless, the present investigations show that a preliminary, two-dimensional design optimization is reasonable for such an optimization task. Furthermore, a sound database of airfoils is available for the three-dimensional design optimization, which significantly reduces the number of required design variables.

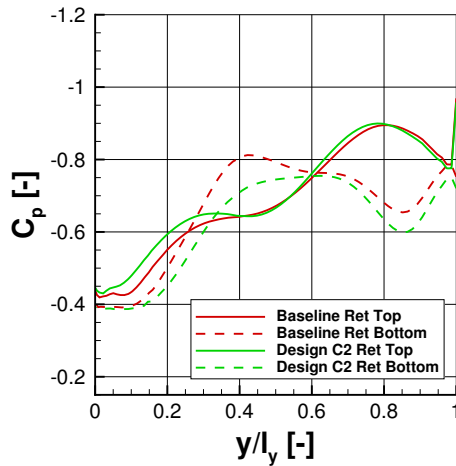
Figure 13 shows the spanwise pressure distribution $C_p(y/l_y)$ for the baseline design as well

as candidate C2. The results are derived from the center of the fairing ($x/c = 0.5$). The station $y/l_y = 0$ corresponds to the most inboard part of the blade-sleeve fairing and $y/l_y = 1$ represents the transition to the rotor-blade. Furthermore, the results for the advancing rotor blade are depicted in Fig. 13a. Between 45 and 75 percent of the fairing length, an almost constant pressure gradient can be observed for the upper surface of both designs. Moreover, the largest pressure difference between the upper and the lower surface is located at approximately 80 percent of the fairing length and design C2 reveals a bigger pressure difference than the baseline design on almost the entire length of the fairing.

Furthermore, a significant pressure difference can be seen in the region $0.5 \leq y/l_y \leq 1$. Hence, the largest lift contribution is provided by this part of the blade-sleeve fairing. Regarding the retreating blade case, which is shown in Fig. 13b, lower pressure differences between the upper and the lower surface are obtained for both geometries. Additionally, the pressure gradient on the upper surface is reduced compared to the advancing blade case. At $y/l_y = 0$, almost the same pressure levels can be found for both cases. Further, design C2 provides a larger pressure difference between the upper and the lower surface in Fig. 13b.



(a) Advancing rotor blade.



(b) Retreating rotor blade.

Fig. 13 : Spanwise pressure distribution $C_p(y/l_y)$ at the center of the fairing ($x/c = 0.5$) for the baseline design and candidate C2.

7 Conclusion

Within the present publication, the three-dimensional aerodynamic design optimization of the RACER blade-sleeve fairing is described and first results of the ongoing optimization process are shown. An isolated rotor head featuring a full-fairing beanie, a blade-sleeve fairing and a truncated rotor blade is examined. Furthermore, the parameterization of the blade-sleeve fairing is realized by four supporting airfoils, which were aerodynamically optimized during previous work in the FURADO project. For each blade-sleeve section, twelve of the best performing airfoils from the two-dimensional design optimization were selected yielding the design variables for the present optimization problem. The shape of the blade-sleeve fairing is modified by replacing the supporting airfoils. The applied objective functions are represented by the maximization of the lift-to-drag ratio for the advancing rotor blade (C_L/C_D) and the minimization of drag (C_{DS}) for the retreating rotor blade. The optimization is conducted by means a multi-objective genetic algorithm and 334 designs have been evaluated so far. In order to be able to measure the performance improvement for a given design, a baseline candidate is generated for comparison. This baseline geometry is composed out of airfoils, which yield the best compromise regarding both objective functions from the two-dimensional design optimization. Additionally, the objective space is evaluated and a detailed view on the best performing geometries is given. In comparison to the baseline design, a maximum increase of $(\Delta C_L/\Delta C_D)_{rel} = 13.6\%$ was observed for the advancing blade case (Design C1) and a reduction of $(\Delta C_{DS})_{rel} = 10.3\%$ could be achieved for the retreating blade case (Design C2). Moreover, design C2 represents the best compromise for both objective functions and it was selected to be investigated in more detail. For this purpose, the sectional shape as well as the chordwise pressure distribution of the second blade-sleeve section (S2) are compared to the baseline design. Additionally, the spanwise pressure distribution is examined at $x/c = 0.5$ for both designs.

Furthermore, a description of the flow field is given for the baseline geometry, which is representative for candidate C2 as well. Therefore, the averaged and normalized axial flow velocity is examined in four chordwise and spanwise slices. In order to determine any three-dimensional effects, a comparison of the two- and three-dimensional simulation results is performed. Therefore, the sectional pressure distributions are derived for the first and the third blade-sleeve section (S1 and S3) of the baseline design.

Acknowledgements

The authors would like to thank the European Union for the funding of the FURADO research project within the framework of Clean Sky 2 under the grant agreement number 685636. Further, the fruitful collaboration and valuable support of the project partner AIRBUS Helicopters is highly acknowledged. Special thanks are addressed to ANSYS and the DLR for providing the flow simulation software. The authors gratefully acknowledge the Gauss Centre for Supercomputing e.V. (www.gauss-centre.eu) for funding this project by providing computing time on the GCS Supercomputer SuperMUC at Leibniz Supercomputing Centre (www.lrz.de).

References

- [1] Breitsamter C., Grawunder M. and Reß R. Aerodynamic Design Optimization for a Helicopter configuration including a Rotating Rotor Head. *Congress of the International Council of the Aeronautical Sciences*, St. Petersburg, Russia, Vol. 29, pp 0686.1-0686.11, 2014.
- [2] Desvigne D. and Alfano D. Rotor-head/Fuselage Interactional Effects on Helicopter Drag: Influence of the Complexification of the Rotor-head Geometry. *European Rotorcraft Forum*, Moscow, Russia, Vol. 39, 2013.
- [3] Graham D.R., Sung D.Y., Young L.A., Louie A.W. and Stroub R.H. Helicopter Hub Fairing and Pylon Interference Drag. *Technical Memorandum Nr. 101052*, NASA-Ames Research Center, Moffet Field, CA, USA, 1989.
- [4] Sheehy T. and Clark D. A Method for Predicting Helicopter Hub Drag. *Final Report Nr. AD-A021 201*, United Technologies Corporation, Stratford, CT, USA, 1976.
- [5] Sung D.Y., Lance M.B., Young L.A. and Stroub R.H. An Experimental Investigation of Helicopter Rotor Hub Fairing Drag Characteristics. *Technical Memorandum Nr. 102182*, NASA-Ames Research Center, Moffet Field, CA, USA, 1989.
- [6] Khier W. Numerical Analysis of Hub and Fuselage Interference to reduce Helicopter Drag. *European Rotorcraft Forum*, Amsterdam, Netherlands, Vol. 38, 2012.
- [7] Khier W. Computational Investigation of Advanced Hub Fairing Configurations to reduce Helicopter Drag. *European Rotorcraft Forum*, Southampton, United Kingdom, Vol. 40, 2014.
- [8] Eurocopter. The X³. *Rotor Journal*, Vol. 88, pp 14-19, 2010.
- [9] Airbus Helicopters. Press-Release Airbus Helicopters 2017. URL: <https://www.airbus.com/newsroom/press-releases/de/2017/06/Airbus-Helicopters-reveals-Racer-high-speed-demonstrator-configuration.html>
- [10] Pözlbauer P., Desvigne D. and Breitsamter C. Aerodynamic Design Optimization of a Helicopter Rotor Blade-Sleeve Fairing. *Deutscher Luft- und Raumfahrtkongress*, Munich, Germany, Vol. 66, 2017.
- [11] Arora J. *Introduction to Optimum Design*. 2nd edition, Elsevier Science, 2004.
- [12] Grawunder M., Reß R., Stein V., Breitsamter C. and Adams N.A. Flow Simulation of a Five-Bladed Rotor Head. *Dillmann, A. and Heller, G. and Krämer, E. and Kreplin, H.-P. and Nitsche, W. and Rist, U. New Results in Numerical and Experimental Fluid Mechanics IX: Contributions to the 18th STAB/DGLR Symposium, Stuttgart, Germany, 2012*, Springer International Publishing, 2014.
- [13] Goldberg D.E. *Genetic Algorithms in Search, Optimization and Machine Learning*. 1st edition, Addison-Wesley Longman Publishing Co., Inc., 1989.

- [14] Kalyanmoy D. *Multi-Objective Optimization Using Evolutionary Algorithms*. John Wiley & Sons, Inc., 2001.
- [15] International Civil Aviation Organization. *Manual of the ICAO standard atmosphere extended to 80 kilometres (262 500 feet)*. 3rd edition, International Civil Aviation Organization, 1993.
- [16] Menter F. Two-Equation Eddy-Viscosity Turbulence Models for Engineering Applications. *AIAA Journal*, Vol. 32, No. 8, pp 1598–1605, 1994.
- [17] ANSYS Inc. *Fluent User Guide v17.0*. Ansys Inc., Canonsburg, PA, USA, 2016.
- [18] Lakshminpathy S. and Togiti V. Assessment of alternative formulations for the specific-dissipation rate in RANS and variable-resolution turbulence models. *AIAA Computational Fluid Dynamics Conference*, Honolulu, Hawaii, Vol. 20, 2011.
- [19] Gerhold T. Overview of the Hybrid RANS Code TAU. *MEGAFLOW - Numerical Flow Simulation for Aircraft Design*, Vol. 89, pp 81–92, 2005.
- [20] Adams B., Ebeida M., Eldred M., Jakeman J., Maupin K. and Monschke J. *Dakota, A Multilevel Parallel Object-Oriented Framework for Design Optimization, Parameter Estimation, Uncertainty Quantification, and Sensitivity Analysis*. v6.4, Sandia National Laboratories, Albuquerque, NM, USA, 2016.

8 Contact Author Email Address

Patrick Pözlbauer

mailto:patrick.poelzlbauer@aer.mw.tum.de

Copyright Statement

The authors confirm that they, and/or their company or organization, hold copyright on all of the original material included in this paper. The authors also confirm that they have obtained permission, from the copyright holder of any third party material included in this paper, to publish it as part of their paper. The authors confirm that they give permission, or have obtained permission from the copyright holder of this paper, for the publication and distribution of this paper as part of the ICAS proceedings or as individual off-prints from the proceedings.